JOURNAL OF PROPULSION AND POWER
Vol. 19, No. 3, May–June 2003

Conservation Coupling Technique for Dynamic Inlet–Engine Analyses

Keith Numbers*
U.S. Air Force Research Laboratory, Wright–Patterson Air Force Base, Ohio 45433
and
Awatef Hamed†
University of Cincinnati, Cincinnati, Ohio 45221

A hybrid method is presented for unsteady analysis of turbine engine propulsion systems. The method is a coupled analysis of the inlet–engine combination, incorporating multidimensional inviscid computational fluid dynamics in the inlet with a one-dimensional dynamic turbomachinery model. The domain coupling technique consists of conservation averaging, which reconciles the dimensional inconsistency and characteristic wave propagation to provide time accuracy. The method is applied to an axisymmetric mixed compression inlet integrated with an eight-stage axial compressor at Mach 2.5 operating conditions. Analysis includes methodology verification, steady-state performance, and dynamic results for two different events. The results indicate that the method is capable of simulating large-amplitude dynamic behavior of coupled supersonic inlet–engine systems.

Nomenclature

A	=	cell face area
a	=	speed of sound
Et	=	total energy
e	=	specific energy
F	=	force source term
h_t	=	total enthalpy
J	=	Riemann invariant
M	=	Mach number
m	=	mass flow
P, p	=	pressure
PR	=	compressor stage pressure ratio
P_t	=	total pressure
Q	=	heat source term
R_c	=	inlet cowl lip radius
r	=	radial coordinate
s	=	entropy
T_t	=	total temperature
t	=	time
u, u_n	=	velocity component normal to cell face
V	=	velocity
v	=	volume
W	=	work source term
W_c	=	corrected weight flow
x	=	axial coordinate
γ	=	gas specific heat ratio
η_c	=	compressor stage efficiency
λ	=	wave speed
ρ	=	density
τ	=	time lag
ω_c	=	corrected rotor speed

Received 10 March 2001; revision received 3 August 2002; accepted for publication 8 November 2002.

*Senior Engineer, Air Vehicles Directorate. Member AIAA.
†Professor, Department of Aerospace Engineering. Fellow AIAA.

Introduction

ASSESSMENT of operability and dynamic response of aircraft turbine engines is an important aspect of their design and development. As efficiency benchmarks increase, stability margins are necessarily reduced. The inlet and compressor components are of particular interest because they are susceptible to disturbances that result in serious disruption of their flow process. The initial response of one component as a result of a disturbance propagates throughout the system, possibly precipitating additional response in the other component.[1–4] Hammershock is a classic example, where the amplitude and duration of the response are a strong function of component interaction.[5–8]

Analytical methods can provide a cost-effective engineering tool for dynamic analysis at both the component and system levels. Component-level analysis of the turbine engine dynamics can be accomplished via one-dimensional finite volume models using actuator disk theory (in conjunction with a description of stage performance characteristics). On the other hand, component-level analysis of the multidimensional inlet flowfield can be accomplished using computational fluid dynamics (CFD). An engine face boundary condition for both analyses usually requires some heuristically prescribed temporal behavior. Fully coupled inlet–engine dynamic analyses have only been accomplished using one-dimensional methods.

A rather obvious advancement to the state of the art is a fully coupled dynamic analysis method that uses multidimensional CFD for the inlet and a dynamic model for the engine as shown in Fig. 1. The use of multidimensional CFD in the inlet provides a capability to conduct coupled inlet–engine analysis for configurations that are not conducive to a one-dimensional analysis. Furthermore, the issue of the engine face boundary condition becomes inconsequential. Such a method requires the development of new techniques to couple the two analytical solutions together at the domain interface. The method must propagate waves through the interface accurately and accommodate the spatial discretization inconsistency between the different component analysis methods.

In the present investigation a new interface coupling method is developed that provides for time-accurate wave propagation between the inlet and compressor domains and resolves the discretization inconsistency. Unsteady flow characteristics are analytically constructed in both domains. The intersection of these characteristics yields a time-accurate estimate of the flowfield at the interface. The characteristics-based procedure ensures that waves propagate in the proper direction. The interface discretization inconsistency

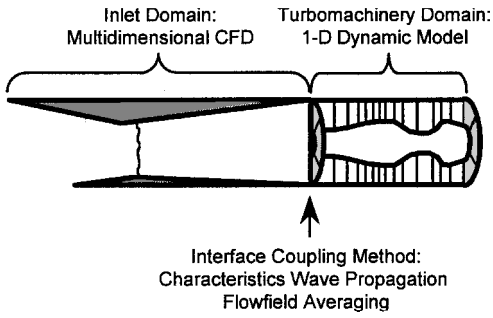

Fig. 1 Coupled inlet–engine dynamic analysis method.

is resolved with a conservative flowfield-averaging method, which represents the inlet domain interface flowfield as a one-dimensional fully mixed equivalent.

Methodology

The current analysis implements a finite volume formulation of the gas dynamic equations of motion. The gas is assumed to be inviscid, compressible, and calorically perfect. Sources terms are included to account for the turbomachinery in the engine domain. The generalized discrete finite volume conservation laws are applied to a polyhedron with N sides (referred to as a "cell"):

$$\Delta v_j \frac{\partial \rho_j}{\partial t} = -\sum_{i=1}^{N} (\rho u_n A)_i + m_j \tag{1}$$

$$\Delta v_j \frac{\partial (\rho \boldsymbol{V})_j}{\partial t} = -\sum_{i=1}^{N} (\rho u_n \boldsymbol{V} + P)_i A_i + \boldsymbol{F}_j \tag{2}$$

$$\Delta v_j \frac{\partial (\rho E_t)_j}{\partial t} = \sum_{i=1}^{N} (\rho u_n E_t + P u_n)_i A_i + W_j \tag{3}$$

where $E_t = \rho(e + V^2/2)$, j refers to the cell centroid, and i refers to polyhedron faces where fluxes and pressure forces occur. W_j, F_j, and m_j are the source terms. In the current analysis axisymmetry was assumed for the flow in the inlet domain, whereas one-dimensional flow was assumed for the engine domain. Additional assumptions and the specific equations of motion for each domain are provided in the Appendix.

Stage Characteristics

The source terms for compressor stages are related to the stage pressure ratio and efficiency, which are functions of the stage characteristics:

$$PR = \frac{P_{t_2}}{P_{t_1}} = f(W_c, \omega_c) \tag{4}$$

$$\eta_c = \frac{h'_{t_2} - h_{t_1}}{h_{t_2} - h_{t_1}} = f(W_c, \omega_c) \tag{5}$$

The steady-state stage characteristics are based on the earlier work of Sugiyama et al.[9] and have the general form shown in Fig. 2. The steady-state stall is at point a. The shape of the pressure ratio and efficiency curves in the unstalled region is specific to the particular compressor being modeled. To the left of point a, the shape of the pressure ratio and efficiency curves in the stalled region is described by three points b, c, and f. Point b corresponds to rotating stall, point c is the minimum pressure ratio in the fully stalled region, and point f defines the shape of the curve in the reverse flow region.

The stage operating point does not respond instantaneously to changes in local corrected weight flow or local corrected rotor speed because of storage of mass, momentum, and energy within the stage volume. To simulate this effect, the instantaneous stage operating condition is assumed to have a linear time-lag response. The form of the time-lag parameter is also shown in Fig. 2. In the stall-free region τ is based on the local characteristic residence time of the

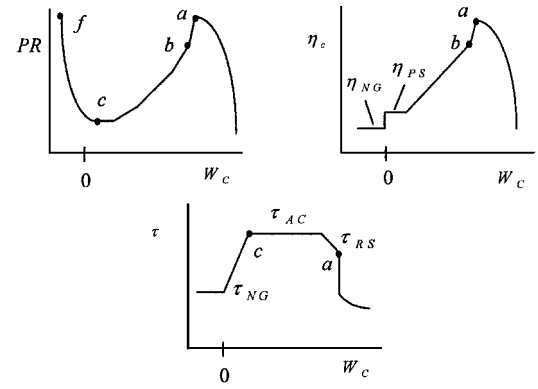

Fig. 2 General form of stage performance characteristics and time constant.

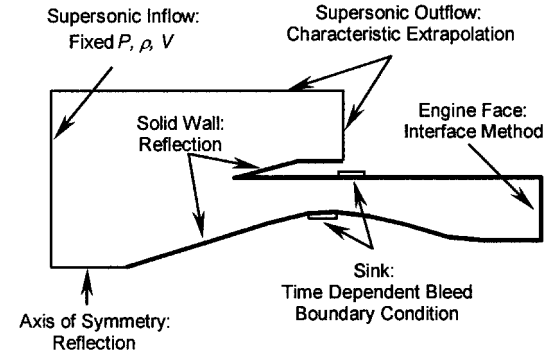

Fig. 3 Typical inlet domain boundary conditions.

stage. In the stalled regime τ is described by points a, b, c, and f and is assumed to be the same for all stages.

Turbomachines have high rotational inertia, which makes the timescale of the rotor dynamics much larger than the gas dynamics. Because the dynamic events being considered are of relatively short duration (20 to 40 ms), the change in physical rotor speed is neglected. However, changes in the local total temperature can result in substantial variation of local corrected rotor speed. The stage characteristics are scaled with corrected rotor speed by assuming that the stage-corrected weight flow varies linearly and the stage enthalpy rise varies with the square of the corrected rotor speed.

The diaphragm upstream of the turbine is typically choked in the type of engine considered in the current investigation. Therefore, the turbine stages and all flowpath components downstream are gasdynamically isolated from the rest of the engine. That is, disturbance waves cannot propagate upstream of the turbine diaphragm. In the present model the turbine diaphragm is simulated by a choked convergent–divergent nozzle.

Numerical Scheme

Second-order spatial accuracy is accomplished by assuming a linear variation of the flow variables in each cell. The linear gradient is determined from a least-squares fit of neighboring cells or the MUSCL scheme of Collela[10] in the inlet and engine domains, respectively.

Jump discontinuities occur at the cell faces, which are resolved with a Riemann solution. This ensures the proper direction of wave propagation and resolves large gradients without dispersive errors. Experience has shown the scheme to be very stable because of the nonlinear properties of the Riemann solution.

Time integration is accomplished by the explicit Runge–Kutta method of Williamson[11] with up to fourth-order accuracy.

Boundary Conditions

Figure 3 shows a typical inlet domain with the boundary conditions identified. At the supersonic inflow boundaries the cell face values are set to the fixed freestream conditions. At supersonic external

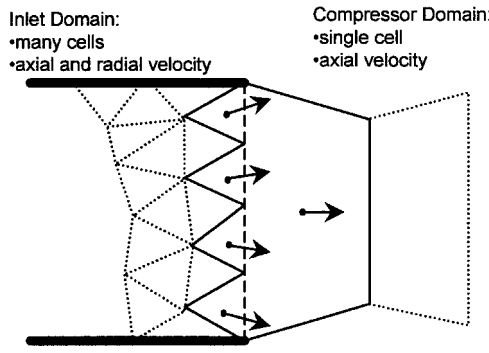

Fig. 4 Schematic of interface cell structure.

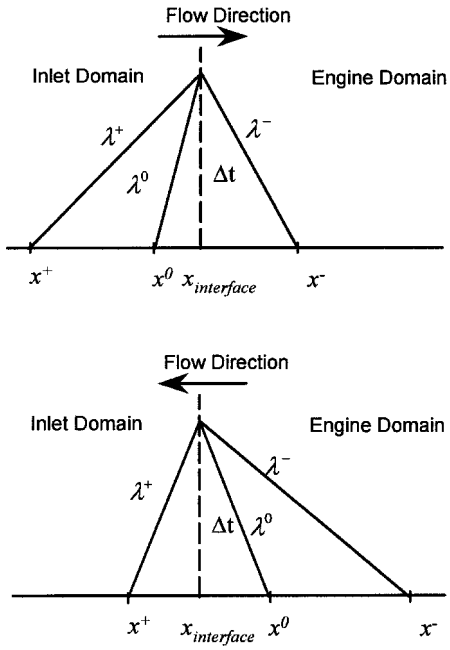

Fig. 5 Schematic of flow characteristics at the interface.

outflow boundaries a nonreflective characteristic-basedcondition is applied. At solid wall boundaries flow tangency is enforced by a reflection condition, and time-accurate bleed boundary conditions are applied at the porous regions. The flow rate through the bleed boundaries changes with time depending upon the local flow condition at the aperture and the pressure maintained in the exhaust plenum. The mass flow through the porous wall region is characterized by a sonic flow coefficient using the data of Sloan.[12] The flow coefficient exhibits the behavior of a choked nozzle.

Boundary conditions in the engine domain consist of the exhaust boundary at the back end. A low-volume convergent–divergent passage is appended to simulate the choked turbine diaphragm. A characteristics-based nonreflective boundary is applied in the case of supersonic outflow at the boundary.

Conservative Interface Coupling Technique

The interface between the inlet domain and the engine domain is a critical element of the entire analysis method. Flow information must be able to pass through this interface in both directions via wave propagation and convection. The problem is complicated by the fact that the two domains being coupled have inconsistent dimensional properties. The technique used here is to couple the domains by characteristic-basedwave propagation (a feature common to the solution techniques of both domains). The dimensional inconsistency is managed with a conservative flow-averaging procedure.

The schematic of the interface is shown in Fig. 4. Several cells of the inlet domain coincide along one face with the much larger foremost cell of the engine domain. Three characteristics are considered: the positive characteristic, the negative characteristic, and the convective or zero characteristic. These characteristics are assumed to be straight lines in the x–t plane having slopes corresponding to the inverse of their corresponding wave speeds.

A schematic of three typical characterisics in the x–t plane at the interface is shown in Fig. 5. The wave speeds λ are a function of the local velocity and acoustic speed:

$$\lambda^+ = (u^+ + a^+), \qquad \lambda^- = (u^- - a^-), \qquad \lambda^0 = u^0 \tag{6}$$

The Riemann invariants are constant along the characteristic lines:

$$J^+ = u^+ + 2a^+/(\gamma - 1), \qquad J^- = u^- - 2a^-/(\gamma - 1)$$
$$s^0 = P^0/(\rho^0)^\gamma \tag{7}$$

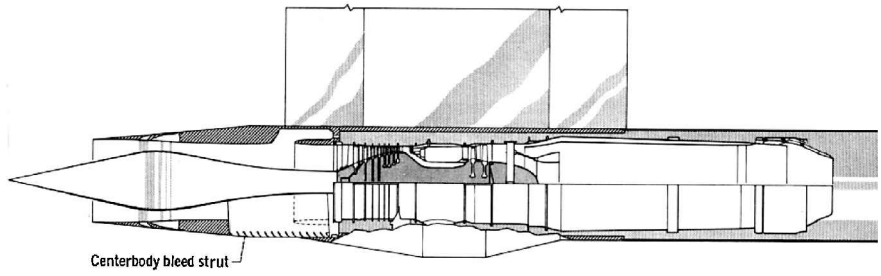

Fig. 6 NASA propulsion system.[1]

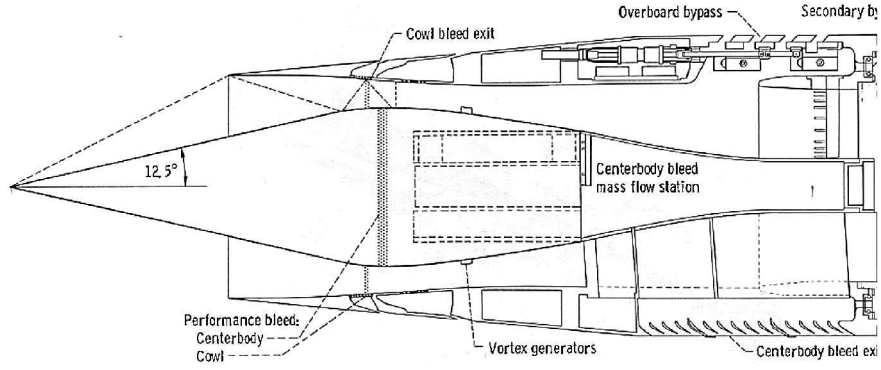

Fig. 7 Inlet geometric details.[1]

The procedure is to track the three characteristic lines that intersect at a desired point on the interface at time $t + \Delta t$ backward in time to their origination points at time t. The Riemann invariants are known at these points and are recombined at the interface at time $t + \Delta t$ to determine the flow state there. This characteristic tracing procedure is repeated for each cell in the inlet domain lying along the interface.

Interface Flux for the Inlet Domain

Assuming the flow is subsonic, the negative characteristic always originates from the foremost cell of the engine domain. In general, it does not intersect the x axis near the cell centroid. Hence, it would be inaccurate to use the cell centroid flow state to form the negative Riemann invariant (J^-). In this case the linear variation of flow properties is employed to get a second-order-accurate determination of this invariant. Because the engine domain flow is one-dimensional, J^- is single valued all along the interface.

Again assuming subsonic flow, the positive characteristic always originates from the cells in the inlet domain. Because the inlet domain cells are an order of magnitude smaller than the engine domain cells, overall accuracy does not suffer by approximating the positive characteristic flow state by the cell centroid values. Unlike the single-valued negative Riemann invariant, the positive Riemann invariant is unique to each cell in the inlet domain.

The zero or convection characteristic could originate from either the inlet domain or the engine domain, depending upon the local flow direction. The local flow direction is determined from the velocity component normal to the interface for each inlet domain cell. The invariant in either case is a statement of constant entropy along the characteristic.

The intersection of the three characteristics at the interface defines the flow state at each face of the inlet domain cells along the boundary:

$$u_{i_{\text{int}}} = (J^+ + J^-)/2 \tag{8}$$

$$a_{i_{\text{int}}} = [(\gamma - 1)/4](J^+ - J^-) \tag{9}$$

$$\rho_{i_{\text{int}}} = \left(a^2_{i_{\text{int}}} \Big/ \gamma s^0\right)^{1/(\gamma-1)} \tag{10}$$

$$P_{i_{\text{int}}} = s^0 \rho^{\gamma}_{i_{\text{int}}} \tag{11}$$

The radial velocity component at the interface is passively convected from the cell centroid values. The subscript i here denotes the individual cell faces of the inlet domain coinciding with the interface. This completes the necessary information to form the fluxes along the interface and integrate the solution in the inlet domain.

Interface Flux for the Engine Domain

The flux for the engine domain cell at the interface must be one-dimensional. The flow state to form this flux is determined from an average of the face values just described for the inlet domain. A conservation-average technique has been selected for this purpose.[13] This technique conserves area, mass flow, stream thrust (integral of momentum and pressure forces), and total energy at the interface and is analogous to inviscid mixing in a constant-area duct. If a nonuniform flow undergoes this idealized process, the fully mixed uniform flow state is the same as the conservation average.

To form the conservation average, the following integral relations are formed:

$$A_{\text{total}} = \sum_{i=1}^{n} A_{i_{\text{int}}} = A_{\text{avg}} \tag{12}$$

$$\dot{m}_{\text{total}} = \sum_{i=1}^{n} \rho_{i_{\text{int}}} u_{i_{\text{int}}} A_{i_{\text{int}}} = \rho_{\text{avg}} u_{\text{avg}} A_{\text{avg}} \tag{13}$$

$$F_{\text{total}} = \sum_{i=1}^{n} \left(P_{i_{\text{int}}} + \rho_{i_{\text{int}}} u^2_{i_{\text{int}}}\right) A_{i_{\text{int}}} = \left(P_{\text{avg}} + \rho_{\text{avg}} u^2_{\text{avg}}\right) A_{\text{avg}} \tag{14}$$

$$\dot{m}_{\text{total}} T_{t_{\text{total}}} = \sum_{i=1}^{n} \rho_{i_{\text{int}}} u_{i_{\text{int}}} T_{t_{i_{\text{int}}}} A_{i_{\text{int}}} = \dot{m}_{\text{total}} \left(T_{\text{avg}} + \frac{u^2_{\text{avg}}}{2C_p}\right) \tag{15}$$

These quantities represent the area, mass, axial stream thrust, and total energy of the flow at the interface. The subscript avg denotes the unique combination of subsonic one-dimensional flow conditions that also satisfy the integrals. The momentum and energy associated with the radial velocity component of flow in the inlet domain are neglected in the conservation average. The averaging error is small as long as the radial velocity component is small compared to the axial component. The average values are used to form the flux at the interface for the engine domain cell, which can then be integrated in time.

Steady-State Results

The present application is an axisymmetric mixed compression supersonic inlet connected to a J85-GE-13 turbojet engine, as shown in Fig. 6. This configuration, tested extensively by NASA,[1,14–16] represents the best available experimental information for comparison purposes. Experimental data are available for various dynamic events at supersonic freestream conditions, including inlet unstarts and compressor surges, and their effects on each other. All of the analyses carried out here corresponds to a nominal freestream Mach number of 2.5.

The inlet shown in Fig. 7 is a Mach 2.5 design with the supersonic flow area contracted 40% externally and 60% internally. The centerbody spike has a 12.5-deg half-angle and can translate to provide starting and off-design operation. The internal cowl lip angle

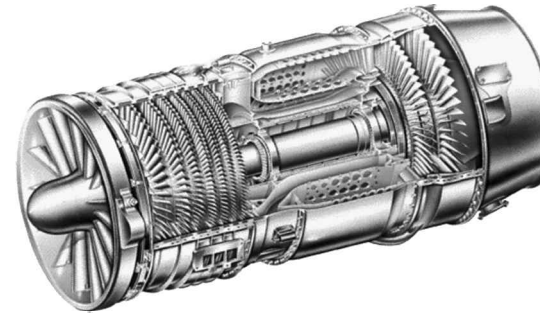

Fig. 8 J85-GE-13 turbojet.

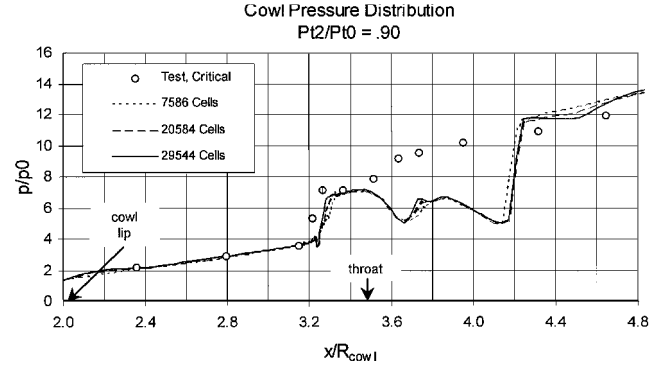

Fig. 9 Inlet domain steady-state solution, static wall pressure traces.

is initially 0 deg, which generates a cowl shock and several shock reflections. The inlet has two bleed regions, one on the cowl at the position of the second shock reflection and another one on the centerbody near the geometric throat. The total bleed flow is nominally 3.5% of the captured mass flow at the design condition. The centerbody is supported by three struts, which divide the duct into three equal circumferential segments all of the way to the engine face. An overboard bypass system is used to match inlet and engine mass flow rates. This bypass flow is collected in a plenum just forward of the compressor and exhausted through three valves to the cowl exterior. A secondary bypass is fed from the same plenum and supplies air for engine cooling through a secondary bypass. The engine cooling air is nominally 3% of the captured mass flow.

The axisymmetry includes the surface geometry as well as the outflow boundaries for the bleed and bypass systems. This results in several simplifications of the actual experimental configuration, which affect the flow solution as follows. First, the centerbody support struts, which represent 11% blockage in the subsonic diffuser, are not modeled. The resultant larger duct cross-section area in the numerical model produces a 12% reduction in the duct Mach number at the steady-state conditions of interest. This in turn affects the propagation wave speeds causing the waves traveling upstream $(u - a)$ to be faster and waves traveling downstream $(u, u + a)$ to be slower. Second, the overboard bypass outflow boundary is modeled as a fully circumferential outlet, rather than the three discrete valves in the experimental configuration. The porosity of the boundary is adjusted in the analysis to reproduce the experimentally observed bypass flow rate. Furthermore, the average Mach number in the bypass plenum is very low. It responds to incoming disturbances like an enclosed volume of stagnated flow. Therefore, the effect of distributed vs discrete bypass outflow on overall disturbance wave propagation is expected to be negligible.

The engine has an eight-stage axial compressor of design pressure ratio 7.0, shown in Fig. 8. The compressor incorporates variable inlet guide vanes and interstage bleed in the third, fourth, and fifth stages. The guide vanes and interstage bleed are controlled as a function of the corrected rotor speed. The compressor is driven by a two-stage turbine. The turbine is followed by an afterburner and a convergent nozzle. The J85 design corrected airflow is 43.3 lbm/s, and the design corrected rotor speed is 16,700 rpm.

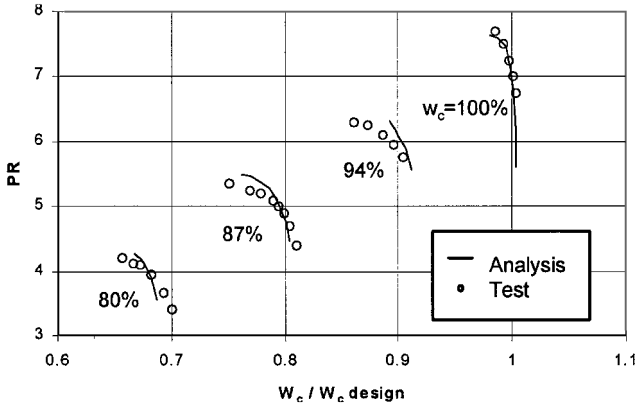

Fig. 10 J85 steady-state compressor map comparison.

Uncoupled Steady-State Analysis

Steady-state solutions of the inlet domain alone were obtained to investigate grid independence. The inlet domain grid spacing was successively reduced until no significant change in the supercritical position of the terminal normal shock. Static wall pressure traces are shown in Fig. 9 for the three grid sizes and compared to the experiment. The 29,544 cell grid shows some improvement in the position of the first cowl shock reflection on the centerbody at $x/R_c = 2.9$. The second shock reflection on the cowl $(x/R_c = 3.2)$ is consistently predicted downstream of the experiment. This is attributed to boundary-layer growth on the centerbody and cowl upstream of the bleeds, which would deflect the shock waves at larger angles. The location of the bleed regions is evident in the numerical solutions by the dip in wall pressure at $x/R_c = 3.4$ on the centerbody and $x/R_c = 3.25$ on the cowl.

Evaluating the results shown in Fig. 9, the terminal shock position changes most from 7586 cells to 20,584 cells, but little difference

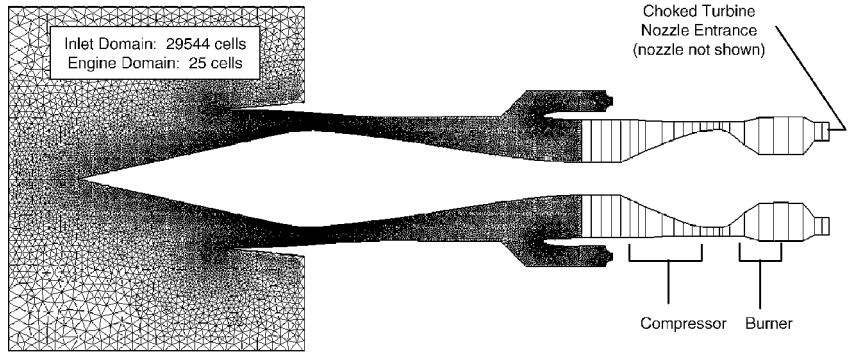

Fig. 11 Combination grid topology.

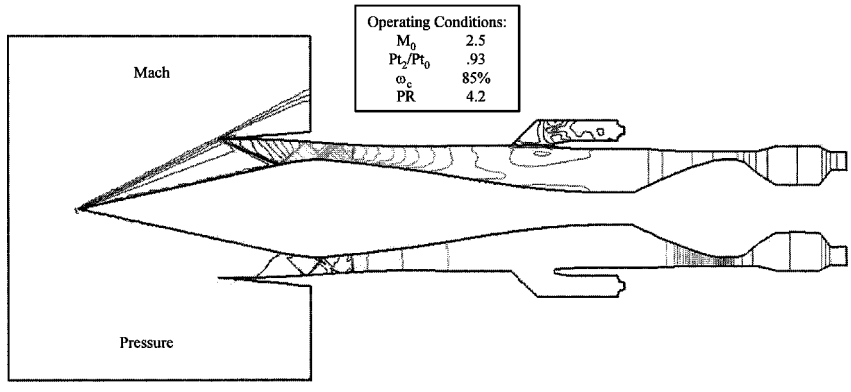

Fig. 12 Coupled steady-state solution.

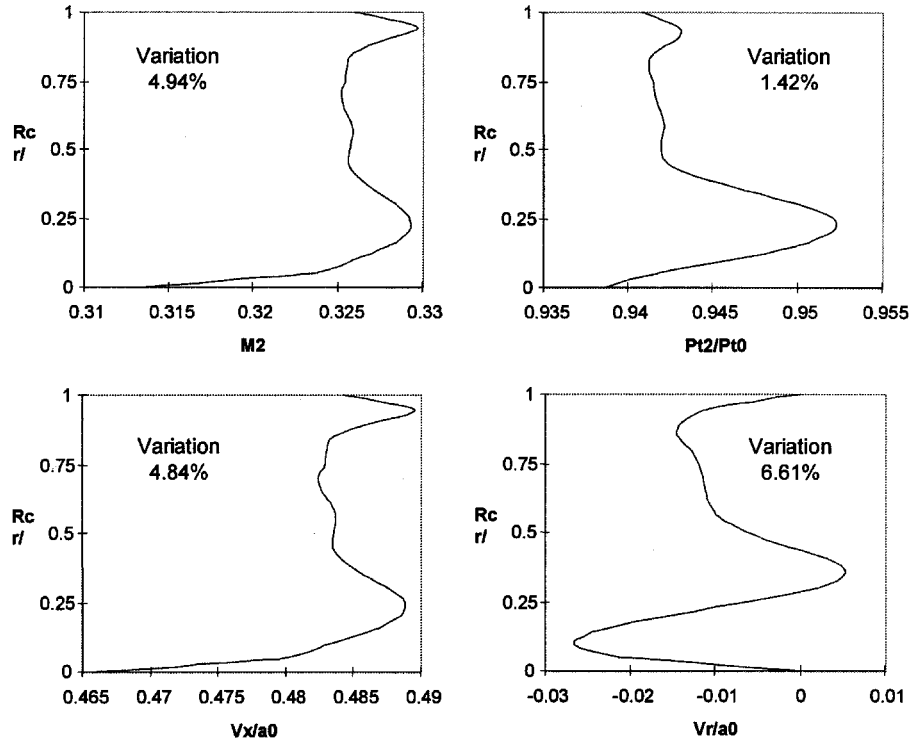

Fig. 13 Steady-state coupled solution interface flow profiles.

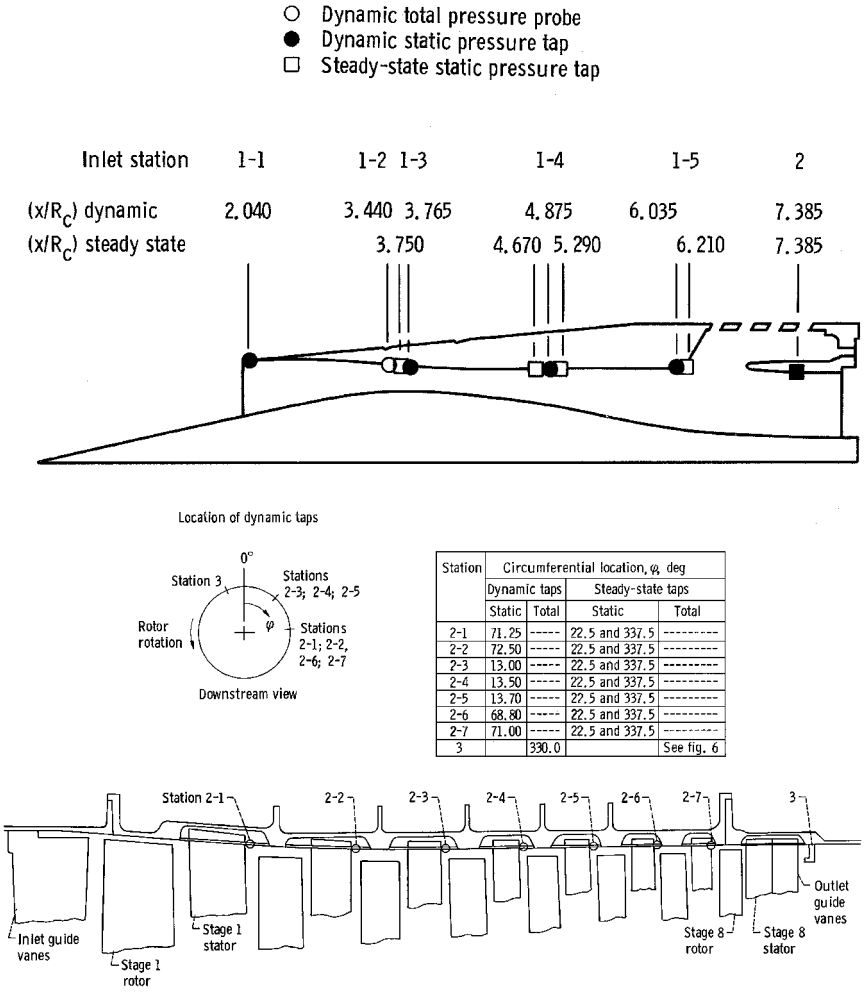

Station	Circumferential location, φ, deg			
	Dynamic taps		Steady-state taps	
	Static	Total	Static	Total
2-1	71.25	-----	22.5 and 337.5	---------
2-2	72.50	-----	22.5 and 337.5	---------
2-3	13.00	-----	22.5 and 337.5	---------
2-4	13.50	-----	22.5 and 337.5	---------
2-5	13.70	-----	22.5 and 337.5	---------
2-6	68.80	-----	22.5 and 337.5	---------
2-7	71.00	-----	22.5 and 337.5	---------
3		330.0		See fig. 6

Fig. 14 NASA experiment instrumentation locations.[1]

Table 1 Inlet domain steady-state results

		No. of cells in numerical grid		
Parameter	Test	7,586	20,584	29,544
Cowl entrance mass flow ratio	~1.0	0.972	0.994	0.983
Cowl bleed mass flow, %	~1.5	0.8176	0.8516	0.8414
Centerbody bleed mass flow, %	~1.5	0.4474	0.4455	0.4351
Overboard bypass mass flow, %	0	0	0	0
Cooling bypass mass flow, %	0	0	0	0
Engine face mass flow ratio	0.975	0.9595	0.9806	0.9705
Terminal shock position, x/R_c	3.4	4.176	4.208	4.208
Engine face total pressure recovery	0.899	0.9265	0.9300	0.9285
Engine face static pressure ratio, $P2/P0$	~15	14.44	14.44	14.44

is achieved by increasing to 29,544 cells. The 29,544 cell grid is selected for further analysis because the increased computational time associated with the smaller grid cell size was not prohibitive. The calculated position of the terminal normal shock ($x/R_c = 4.2$) is considerably farther downstream of the experimentally observed location (about $x/R_c = 3.4$). This discrepancy is caused by the viscous interactions not included in the inviscid solution. Furthermore, experimental inlet total pressure loss is composed of shock losses and viscous losses. If the calculated total pressure loss is to match the experiment, the terminal shock will be positioned further downstream in an inviscid solution. This increases the shock Mach number and the total pressure loss, which supplants the missing viscous loss.

Inlet performance parameters are listed in Table 1 for the experiment and the three grid sizes. The bypass valves for this case are closed such that there is no flow through the bypass exhaust apertures. The mass flow rates (cowl entrance, bleed, or engine) vary slightly with the grid refinement (4% maximum variation). The effect of the grid on the mass flow was not fully explored. Although this is normally not acceptable for a steady-state performance analysis, it was felt to be sufficient to demonstrate the subsequent dynamic analysis capability of the method. The pressure recovery is insensitive to grid refinement (0.4% maximum variation). The calculated total bleed flow rate is considerably less than the experimentally observed value reported to be 2.5–3.5% in several of the NASA references. This difference is caused by the calculated terminal normal shock position. The measured terminal normal shock position is at the location of the centerbody bleed region, such that the local pressure is higher, and therefore the bleed flow rate is higher. The computed engine face mass flow ratio is in good agreement with the experiment. The computed total pressure recovery is slightly higher than the experiment (about 3%).

The computed supercritical shock position will have an impact on the prediction of the dynamic events because these steady-state results are the nominal initial condition. The propagation of disturbance waves is effected by the local velocity and speed of sound. To illustrate this impact, a shock wave is assumed to be traveling upstream in the supersonic portion of the flow. It is further assumed that this shock wave has sufficient strength to stagnate the flow in the duct behind it. This is a good approximation for a compressor surge hammershock. The upstream propagation Mach number M_p of this wave is given by

$$M_p = \{1 + [M(\gamma + 1)/4]^2\}^{\frac{1}{2}} + M[(\gamma + 1)/4 - 1] \qquad (16)$$

where M is the Mach number of the flow into which the shock is travelling.[7] The upstream propagation speed V_p is then

$$V_p = M_p a \qquad (17)$$

Taking the derivative of Eq. (16) reveals that the shock upstream propagation Mach number is a minimum when $M = 1.4907$. For the inlet configuration under consideration, the average Mach number in the supersonic diffuser is about 1.5. The temperature is also relatively low in the supersonic diffuser. Hence, the upstream propagation speed is slowest in the supersonic diffuser portion of the inlet. Therefore, it will take longer for a disturbance to propagate

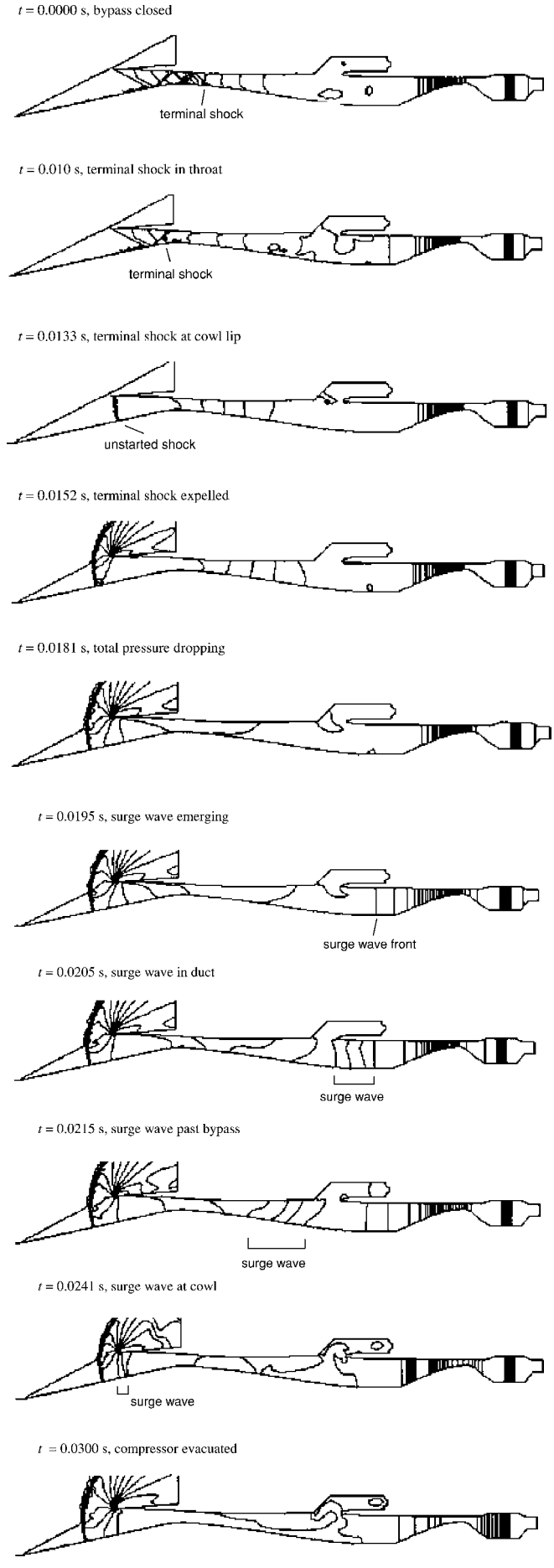

Fig. 15 Case 1—density contours.

from the terminal normal shock position to the cowl lip when the inlet is highly supercritical. This impact is partially offset by the increased upstream propagation speed in the subsonic portion of the duct because the computed Mach number is lower than the experiment (as a result of the exclusion of the centerbody support strut blockage).

Steady-state solutions of the engine domain are obtained for a range of mass flow rates and rotor speeds. Figure 10 shows the J85 compressor map comparing the computed performance with that documented by Milner and Wenzel.[17] The model reproduces the constant speed performance lines and stall points with acceptable accuracy. The stall point for the current analysis is considered to be when any one of the stages enters into the stall regime. The current engine model results are found to be identical to the original model of Sugiyama et al.[9]

Coupled Steady-State Analysis

Figure 11 shows the combined grid for the numerical model with the 29,544 cell inlet domain and the one-dimensional cell arrangement for the engine domain. The conditions for the steady-state solution are Mach 2.5, inlet recovery 93%, corrected rotor speed 85%, and compressor pressure ratio 4.2. Mach number and pressure contours are shown in Fig. 12. Integral and average quantities at the interface are listed in Table 2. Conservation of mass, axial stream thrust, and total energy are achieved per the conservation average. Also noted is the negligible radial momentum component in the inlet domain. This is the primary reason for the good match in Mach, static pressure, and total pressure across the interface, which is not required by the averaging procedure. Figure 13 shows the profiles of the Mach number, total pressure, and velocity components at the interface from the inlet domain solution. The pressures are referenced to freestream total pressure, and the velocity components are referenced to freestream speed of sound. The "maximum minus minimum" variation of each flow parameter is also given. These data are provided to show that the profiles in the inlet solution are not driven to be uniform at the engine face. Rather, the profiles are a result of the local inlet domain characteristics interacting with the average engine domain characteristic per the interfacing procedure. It is not expected that these profiles are comparable to experimental profiles because the inlet flow solution is inviscid.

Coupled Dynamic Analysis

Two cases of coupled dynamic analysis are presented here to demonstrate the dynamic response capability of the method. These events involve large-amplitude dynamic response initiated by either a compressor surge or an inlet unstart. In both cases the effect of the initial disturbance in one component causes the other component to become unstable. The interaction between components is not a small disturbance phenomenon.

The simulated propulsion system is the axisymmetric mixed compression supersonic inlet connected to a J85-GE-13 turbojet engine shown in Figs. 6 and 7. The reference data[1,14–16] represent the best available experimental information for comparison purposes. All of the analyses carried out here correspond to a nominal freestream Mach number of 2.5. The pressure recording stations in the experimental apparatus are shown in Fig. 14. These will be referred to in the following sections.

Table 2 Interface flow quantities

Quantity	Inlet domain	Engine domain	Conservation error
Area, ln.^{2}	184.27	184.27	0%
Mass, lbm/s	32.46	32.49	0.09%
Axial stream thrust, lb	3260	3261	0.03%
Total energy, BTU	5477	5482	0.09%
Axial momentum, lb	423.1	423.9	Not conserved
Radial momentum, lb	−8.2	0	Not conserved
Average Mach	0.3264	0.3267	Not conserved
Average pressure, psi	15.396	15.397	Not conserved
Average total pressure, psi	16.576	16.579	Not conserved

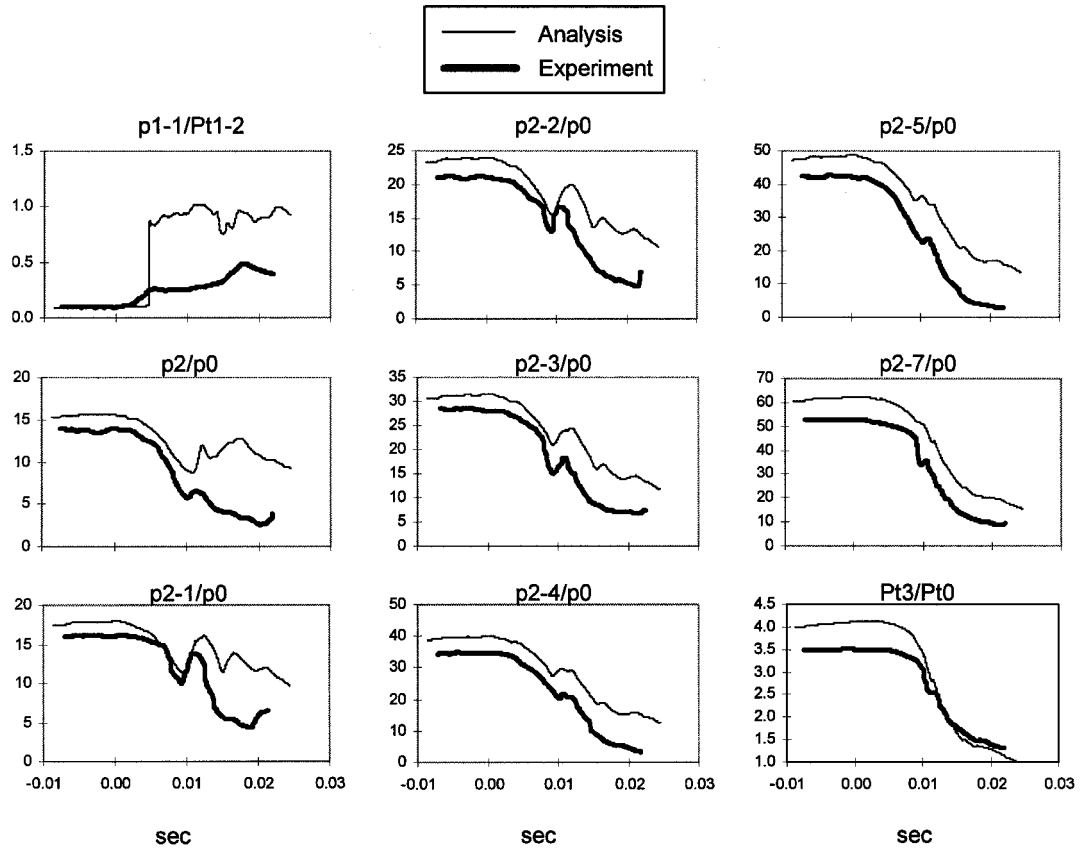

Fig. 16 Case 1—pressure traces.

Dynamic Simulation—Case 1

Case 1 of dynamic simulation is an inlet unstart triggered by reducing the overboard bypass flow. The experimentally observed phenomena occur as follows. The reduction of bypass flow causes the inlet to supply too much corrected mass flow to the engine. The inlet flow adjusts by moving the terminal normal shock toward the throat, which raises the total pressure recovery and lowers the corrected mass flow. However, the shock becomes unstable in the throat and the inlet unstarts. The inlet unstart results in a large drop in total pressure at the engine face, which causes the instantaneous compressor pressure ratio to exceed the stall limit. A subsequent compressor surge develops and propagates forward through the inlet until both the inlet and compressor are evacuated of high-pressure air.

The initial steady-state operating conditions are listed here: Mach is 2.5; $Pt2/Pt0$ is 0.93; ω_c (% design) is 85; and PR is 4.51. The reduction of overboard bypass flow is accomplished by parametrically reducing the porosity (area) at the outflow boundary. The reduction of porosity is taken in small steps (a few percent change for each step), and the solution is integrated in time to a steady state after each change. The position of the terminal shock is monitored as it moves upstream to the throat. The final step triggers the inlet unstart, and the solution is allowed to proceed without further intervention. This procedure is intended to simulate the experimental procedure, in which the overboard bypass valve was closed in a quasi-steady manner until the unstart occurred.

Density contours of the dynamic simulation at various instances in time are shown in Fig. 15. Time zero in this figure corresponds to the instant when the final bypass porosity reduction occurs, with the terminal normal shock in a near critical position. A relatively long period of 10 ms is seen before the terminal shock moves upstream of the throat. After an additional 3.3 ms, this shock is at the cowl station. The next two frames ($t = 15.2$ ms, 18.1 ms) show the unstart condition with the inlet duct evacuating. This results in total pressure drop at the engine face and instantaneous exceedance of the compressor surge pressure ratio. At 19.5 ms the surge wave is eminating from the compressor. The entire surge wave is evident just aft of the bypass opening at 20.5 ms. The surge wave moves forward of the bypass opening at 21.5 ms, and a pressure pulse is also seen propagating in the bypass plenum. As the surge wave propagates forward in the inlet, it coalesces into a shorter wavelength, $t = 24.1$ ms. Finally at 30 ms the surge wave is expelled from the inlet.

Pressure histories for this simulation are shown in Fig. 16. These are compared to the experimental data of Choby et al.[1] The data consist of static and total pressures at several stations in the compressor, static pressure at the engine face, and the ratio of cowl static pressure to inlet throat total pressure. (This ratio is used as the primary indicator of inlet unstart in the experiment.) The computed pressure histories are in fair agreement with the experimental data. Because the experiment has an arbitrary start time, the computed results are synchronized with experiment by the condition where the cowl static to throat total pressure ratio ($p1\text{-}1/Pt1\text{-}2$) rises by 1%. (Note: This should not be confused with time zero for Fig. 3). The pressure ratio ($p1\text{-}1/Pt1\text{-}2$) has a slight increase at time zero (by definition) as the terminal shock passes forward of station 1-2, which slightly lowers $Pt1\text{-}2$ in the denominator. The second larger increase is caused by the terminal shock passing forward of the cowl, which greatly increases $p1\text{-}1$ in the numerator. There is marked difference between the computational and the experimental trace for this parameter ($p1\text{-}1/Pt1\text{-}2$), which is attributed to the viscous effects. The measured initial rise is more gradual, which might be caused by pressure feeding forward through the subsonic boundary layer. Also, the measured overall rise is less than the computed values, which again is attributed to viscous interaction not simulated by the inviscid calculation.

The pressure history within the compressor is characterized by a gradual drop in all stages. However, the pressure drops in the forward stages faster than in the aft stages, such that the instantaneous pressure ratio rises above the stall line. A surge is initiated at about 90 ms, with a surge wave forming in the forward compressor stages. The amplitude of the surge wave is attenuated in the aft stages. In

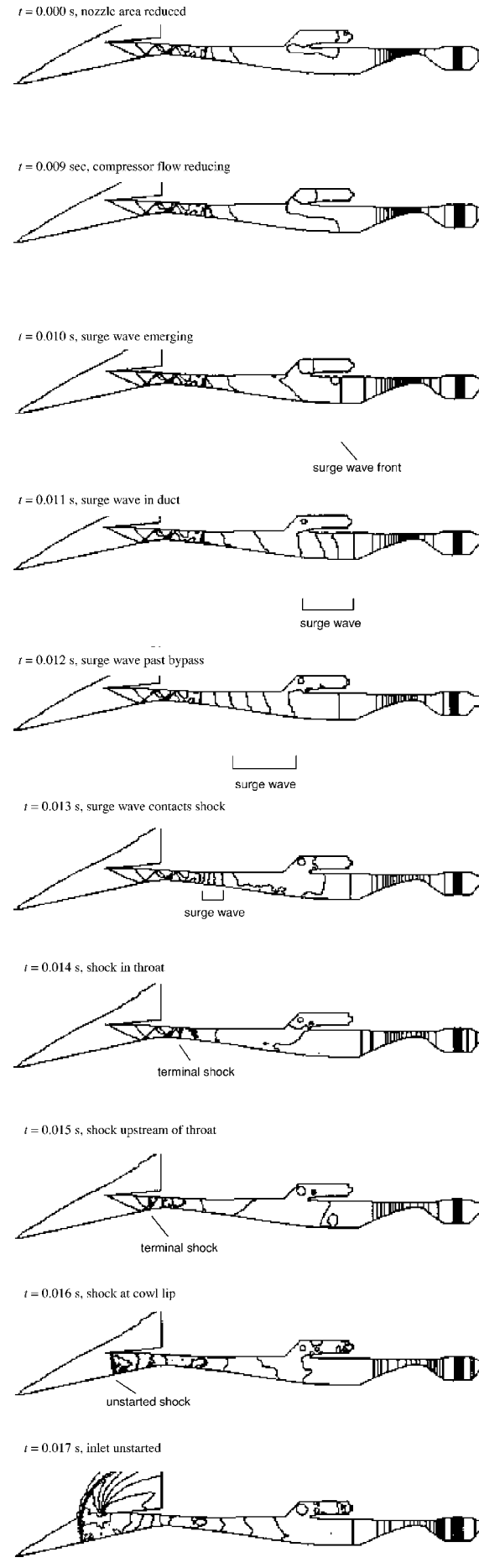

Fig. 17 Case 2—density contours.

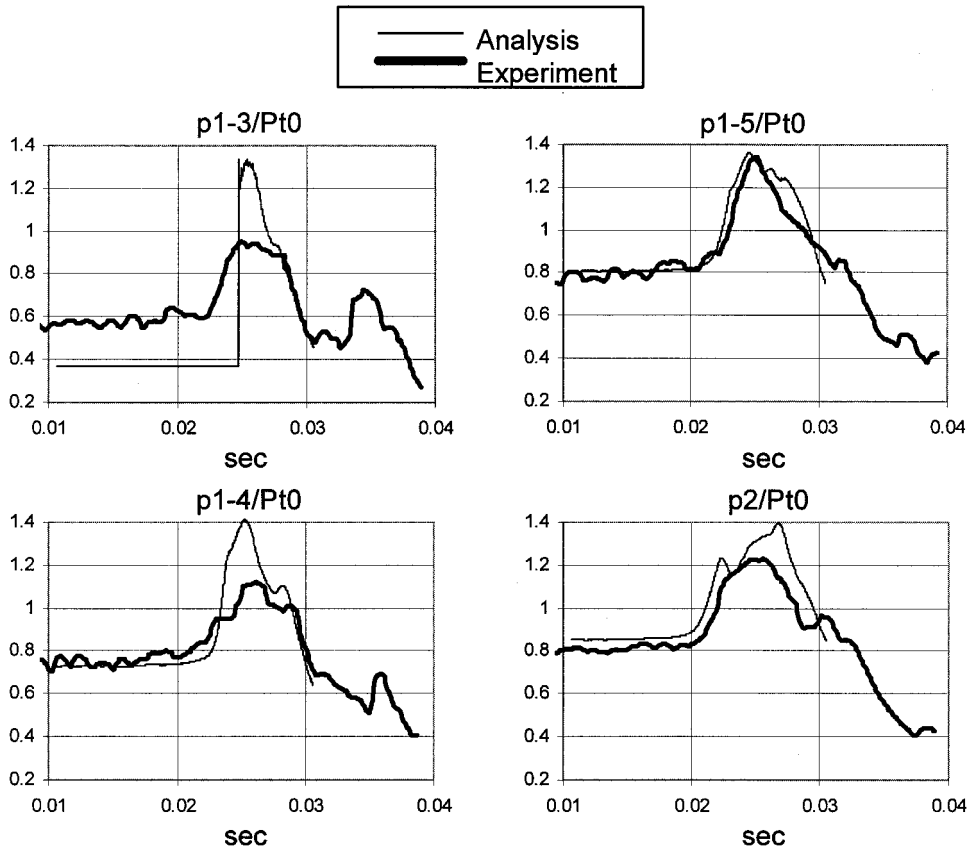

Fig. 18 Case 2—pressure traces.

general, the computed transient through the compressor has a lag of about 3 ms for the peak of the surge wave, compared to the experiment.

Dynamic Simulation—Case 2

Case 2 of dynamic simulation is a compressor stall forced by reduction of the corrected mass flow. The experimentally observed phenomena occur as follows. Reducing the corrected mass flow at constant rotor speed raises the compressor overall pressure ratio until the stall line is exceeded. The compressor stall results in a strong surge wave, which propagates forward through the inlet duct. The surge wave interacts with the terminal normal shock, which cannot support the instantaneous local pressure rise. The terminal normal shock is driven ahead of the throat to unstart the inlet.

The initial steady-state operating conditions are listed here: Mach is 2.5; $Pt2/Pt0$ is 0.90; ω_c (% design) is 88; and PR is 5.61. The mass flow reduction is accomplished by decreasing the engine model nozzle area in small steps similar to the procedure just discussed for the bypass area reduction. The area change for each step is on the order of a few percent. This procedure is intended to simulate the experimental procedure in which the primary exhaust of the turbojet was closed in a quasi-steady manner until the compressor stalled.

Density contours of the dynamic simulation at various instances in time are shown in Fig. 17. Time zero in this figure corresponds to the instant when the final nozzle closure occurs. The total event occurs in only 17 ms, compared to 30 ms for case 1. At 10 ms the surge wave front is emerging from the compressor face. The surge wave propagates to the terminal normal shock position at 13 ms. The terminal shock is expelled forward to the cowl at 16 ms, and the unstart is complete at 17 ms.

Although it is not evident in the density contour frames, the overboard bypass plenum has significant interaction with the surge wave as is passes by the bypass opening. Part of the surge wave propagates into the plenum, which serves to reduce the magnitude of the portion of the wave continuing forward through the inlet duct. The pressure wave transmitted into the bypass plenum reflects off of the choked outflow boundary and returns to the duct.

The pressure histories for this simulation are shown in Fig. 18. These are again compared to the experimental data of Choby et al.[1] In this case the data consist of static pressures at various stations throughout the inlet duct and at the engine face. The computed pressure histories are in fair agreement with the experimental data. The computed results are synchronized in time with the experiment by equating the instant when the engine face pressure ($p2/Pt0$) increases by 5% at $t = 0.02$ ms. The computed time of surge wave peak pressure matches the experiment quite well. As in case 1, the computed pressure trace at station 1–3 (the throat station) is compromised by the inviscid calculation. Again, the measured pressure rises more gradually and has reduced amplitude. This is explained by the difference in the initial terminal shock position between the experiment and the calculation. The experimental initial terminal shock position is forward of station 1–3, such that the surge wave travels in subsonic flow and has not coalesced into a shock. The computational initial terminal shock position is aft of station 1–3, such that the surge wave coalesces with the terminal shock prior to reaching station 1–3. This coalesced shock produces the instantaneous pressure rise as it passes forward of station 1–3 in the computed results.

Conclusions

A new method is developed for coupled inlet–engine dynamic analysis of turbomachinery-based propulsion systems. The primary advancement is the integration of multidimensional computational fluid dynamics in the inlet domain with a validated one-dimensional dynamic engine model in the turbomachinery domain. The combination provides higher fidelity geometric simulation of the inlet than previous strictly one-dimensional methods. The method is demonstrated to be capable of simulating large-amplitude, low-frequency disturbances in the form of inlet unstarts and compressor surges. The interfacing procedure using unsteady flow characterisitics and

conservation averaging is shown to be a feasible approach to couple the inlet domain to the engine domain for dynamic analyses.

The method is applied to an axisymmetric mixed compression inlet connected to a turbojet engine. A steady-state solution indicates that excellent conservation of mass, momentum, and energy is achieved with the interfacing procedure. In comparison to the available experimental data for two different dynamic events, reasonable accuracy was obtained. The coupled analysis method exhibits good ability to predict wave propagation through the interface. Unstart waves and surge waves are tracked in time with good accuracy. Some discrepancies in peak amplitude are noted, particularly in the throat region of the inlet. It is considered that these discrepancies are a result of viscous interactions not presently simulated by the inlet domain flow solver, rather than the overall coupled analysis approach.

Anticipated improvements in the method include viscous inlet analysis and more sophisticated turbomachinery models. It is not expected that viscous inlet analysis will improve the wave propagation prediction because this is an inviscid phenomenon. However, the viscous analysis would improve the ability to establish initial conditions and wall pressure response for inlets that have dominant viscous interactions in their throat regions. Incorporation of a compressor model with circumferential and/or radial flow component capability would improve the results of both steady-state and dynamic coupled analysis.

Appendix: Equations of Motion

For the inlet domain the governing conservation equations are applied in cylindrical coordinates to five-sided finite volumes, as shown in Fig. A1. The resulting discrete conservation laws are

$$\Delta v_j \frac{\partial \rho_j}{\partial t} = -\sum_{i=1}^{3} (\rho u_n A)_i \tag{A1}$$

$$\Delta v_j \frac{\partial (\rho V_x)_j}{\partial t} = -\sum_{i=1}^{3} (\rho u_n V_x + P)_i A_i \tag{A2}$$

$$\Delta v_j \frac{\partial (\rho V_r)_j}{\partial t} = -\sum_{i=1}^{3} (\rho u_n V_r + P)_i A_i + P_j \Delta A_{\text{axi}} \tag{A3}$$

$$\Delta v_j \frac{\partial (\rho E_t)_j}{\partial t} = \sum_{i=1}^{3} (-\rho u_n E_t + P u_n)_i A_i \tag{A4}$$

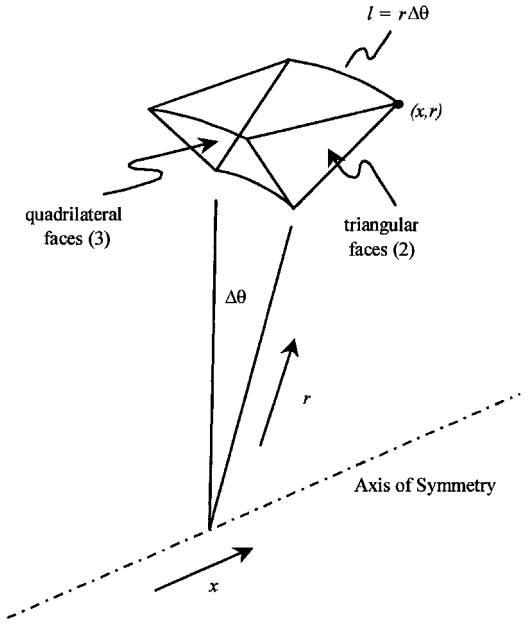

Fig. A1 Inlet domain finite volume schematic for axisymmetric geometry.

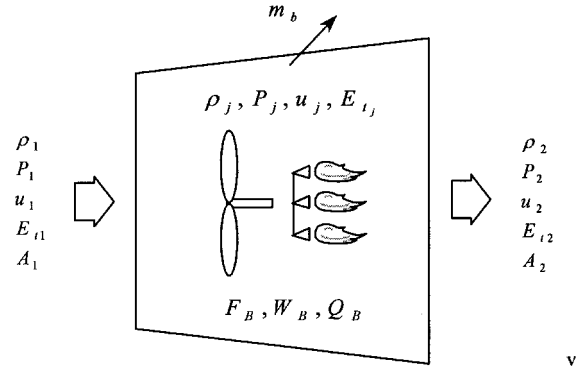

Fig. A2 Engine domain control volume.

Note the summation involves only three sides of the volume because the axisymmetry eliminates flux terms on the faces parallel to the axis of symmetry. Pressure force terms act radially on these faces via ΔA_{axi}, which is the lateral area change upon which P_j.

For the engine domain the flow is assumed to be quasi-one-dimensional with actuator disk source terms representing the turbomachinery. The direction of flow is assumed parallel to the engine centerline axis and mass averaged at any cross section. Viscous effects in the turbomachinery (frictional losses and flow separation on the blades or casing walls) are taken into account in the stage performance characteristics. A typical control volume is shown in Fig. A2. The possibility of contained turbomachinery, bleed mass extraction, and heat addition through burning are shown. The resulting discrete conservation laws are

$$\Delta v_j \frac{\partial}{\partial t}(\rho_j) + [(\rho u A)_2 - (\rho u A)_1] + m_{\text{bj}} = 0 \tag{A5}$$

$$\Delta v_j \frac{\partial}{\partial t}(\rho_j u_j) + \left[(\rho u^2 A)_2 - (\rho u^2 A)_1\right] + m_{\text{bj}} u_j = [(PA)_1 - (PA)_2 + P_j(A_2 - A_1)] + F_B \tag{A6}$$

$$\Delta v_j \frac{\partial}{\partial t}(E_{t_j}) + [(uE_tA)_2 - (uE_tA)_1] + m_{\text{bj}} h_{\text{ij}} = [(PuA)_1 - (PuA)_2] + W_B + Q_B \tag{A7}$$

where subscripts 1 and 2 refer to the front and aft stations of the stage, respectively. The P_j term in the momentum equation accounts for pressure forces on the lateral areas of the control volume acting in the axial direction. The source terms for turbomachinery are F_B and W_B. The source term for heat addition because of combustion is Q_B. Source terms for bleed mass extraction are indicated by the bleed mass flow rate m_b. The blade force and work terms for a compressor stage are determined from the momentum and energy equations under the assumption of steady, constant mass flow conditions:

$$F_B = \dot{m}_j(u_2 - u_1) + (PA)_2 - (PA)_1 - P_j(A_2 - A_1) \tag{A8}$$

$$W_B = \dot{m}_j\left[\left(e_2 + u_2^2/2\right) - \left(e_1 + u_1^2/2\right)\right] + (u_2 P_2) - (u_1 P_1) = \dot{m}_j\left(h_{t_2} - h_{t_1}\right) \tag{A9}$$

It is assumed that a stage consists of a rotor and stator pair, both contained within a single control volume.

References

[1] Choby, D., Burstadt, P., and Calogeras, J., "Unstart and Stall Interactions Between a TurboJet Engine and an Axisymmetric Inlet with 60% Internal Area Contraction," NASA TM X-2192, March 1971.

[2] Reukauf, P. J., "Flight-Measured Transients Related to Inlet Performance on the YF-12 Airplane," NASA CP 2054, 1978, pp. 435–438.

[3] Nugent, J., and Holzman, J. K., "Flight-Measured Inlet Pressure Transients Accompanying Engine Compressor Surges on the F-111A Airplane," NASA TN D-7696, 1974.

[4] Martin, A. W., and Beaulieu, W. D., "XB-70 Flight Test Data Comparisons with Simulation Predictions of Inlet Unstart and Buzz," NASA CR-1631, June 1970.

[5]Goble, B. D., King, S., Terry, J., and Schoop, M., "Inlet Hammershock Analysis Using a 3-D Unsteady Euler/Navier–Stokes Code," AIAA Paper 96-2547, July 1996.

[6]Miller, D. N., and Hamstra, J. W., "A Computational Assessment of Surge-Induced Inlet Overpressure Distribution for Preliminary Design," American Society of Mechanical Engineers, 96-GT-548, June 1996.

[7]Kurkov, A. P., Soeder, R. H., and Moss, J. E., "Investigation of the Stall Hammershock at the Engine Inlet," *Journal of Aircraft*, Vol. 12, No. 4, 1975, pp. 198–204.

[8]Young, L. C., and Beaulieu, W. D., "Review of Hammershock Pressures in Aircraft Inlet," *Journal of Aircraft*, Vol. 12, No. 4, 1975, pp. 210–216.

[9]Sugiyama, Y., Tabakoff, W., and Hamed, A., "J85 Surge Transient Simulation," *Journal of Propulsion and Power*, Vol. 5, No. 3, 1989, pp. 375–381.

[10]Colella, P., "A Direct Eulerian MUSCL Scheme for Gas Dynamics," *SIAM Journal of Scientific and Statistical Computing*," Vol. 6, No. 1, 1985, pp. 104–117.

[11]Williamson, J. H., "Low Storage Runge-Kutta Schemes," *Journal of Computational Physics*, Vol. 35, 1980, pp. 48–56.

[12]Sloan, M., "Experimental Bleed Hole Data Base," Inlet Bleed Technology Workshop, NASA Lewis Research Center, Cleveland, OH, Sept. 1993.

[13]McLafferty, G. H., "A Generalized Approach to the Definition of Average Flow Quantities in Nonuniform Streams," United Aircraft Corp. Research Dept., UAC-R-13534-9, July 1954.

[14]Cubbison, R. W., Meleason, E. T., and Johnson, D. F., "Effect of Porous Bleed in a High-Performance Axisymmetric, Mixed-Compression Inlet at Mach 2.50," NASA TM X-1692, Nov. 1968.

[15]Cole, G. L., Neiner, G. H., and Crosby, M. J., "An Automatic Restart Control System for an Axisymmetric Mixed Compression Inlet," NASA TND-5590, Dec. 1969.

[16]Hingst, W. R., and Towne, C. E., "Comparison of Theoretical and Experimental Boundary-Layer Development in a Mach 2.5 Mixed-Compression Inlet," NASA TM X-3026, April 1974.

[17]Milner, E. J., and Wenzel, L. M., "Performance of a J85-13 Compressor with Clean and Distorted Inlet Flow," NASA TM-X-3304, NASA Lewis Research Center, Dec. 1975.